Trailed vorticity modeling for aeroelastic wind turbine simulations in stand still

Georg Pirrung[1], Helge Madsen[1] and Scott Schreck[2]

[1] Wind Energy Department, Technical University of Denmark, Frederiksborgvej 399, DK-4000 Roskilde, Denmark

[2] National Renewable Energy Laboratory, 15013 Denver West Parkway, Golden, CO 80401, USA

E-mail: gepir@dtu.dk

Abstract. Current fast aeroelastic wind turbine codes suitable for certification lack an induction model for standstill conditions. A trailed vorticity model previously used as addition to a blade element momentum theory based aerodynamic model in normal operation has been extended to allow computing the induced velocities in standstill. The model is validated against analytical results for an elliptical wing in constant inflow and against stand still measurements from the NREL/NASA Phase VI unsteady experiment. The extended model obtains good results in case of the elliptical wing, but underpredicts the steady loading for the Phase VI blade in attached flow. The prediction of the dynamic force coefficient loops from the Phase VI experiment is improved by the trailed vorticity modeling in both attached flow and stall in most cases. The exception is the tangential force coefficient in stall, where the codes and measurements deviate and no clear improvement is visible.

1. Introduction

State-of-the-art aeroelastic wind turbine codes that are suitable for simulating the many time series needed for certification typically use an aerodynamics model based on Blade Element Momentum (BEM) theory. These BEM based models can be extended by tip loss corrections and so-called dynamic inflow models that take the wake inertia into account. With this extension, they are suitable to predict the varying induced velocities in an unsteady aeroelastic simulation. In addition to the dynamic induced velocities, there are also dynamic effects due to shed vorticity and dynamic stall, which occur on faster time scales than the dynamic inflow and are typically taken into account by 2D unsteady airfoil aerodynamics models, in this work the one described in [1].

Thus both the larger scale wake effects and the smaller scale unsteady airfoil aerodynamics are taken into account if the turbine is in operation. In standstill, however, BEM theory can not be used, because the basic assumption in BEM, that the rotor can be approximated by a disc, is violated. Therefore the induced velocities due to the vortices trailed from the blades are not modeled, which results in both a wrong steady state load distribution and missing dynamics.

Wind turbine blades are twisted to ensure a reasonable angle of attack distribution along the blade in operation. In standstill, on the other hand, the blade twist leads to large load variations along the blade, and thus strong trailed vorticity that is not modeled in the aeroelastic codes used for wind turbine certification. Further, the inflow turbulence, which in normal operation only affects a part of the relative flow velocity at the airfoils (the other part being due to rotor rotation), causes very large dynamic variations in angle of attack (AOA) along the blade in stand still.

In this work, a trailed vorticity model, which was originally designed for normal operation and implemented as part of a BEM based model in HAWC2, [2, 3, 4], has been extended so that it can be used in standstill conditions. Results from this extended model are compared to the analytical constant downwash at an elliptical wing and measurements from the NREL/NASA Phase VI unsteady experiment, [5].

2. Near wake model description

The near wake model (NWM) for trailed vorticity was originally developed for use in helicopter aerodynamics. It was assumed in the original model that the trailed vorticity stays in the rotor plane. In order to save computation time, the decreasing induction due to a vortex element trailed at a certain position evaluated at a blade section as it moves away from the blade is approximated using two exponential functions. This makes it possible to use an indicial function algorithm to avoid the time consuming numerical integration of vortex arcs based on the Biot-Savart law. The model has since been modified to enable the computation of the induction due to trailed helical vortex arcs, [3], which is important in normal operation at high wind speed. Further, it has been shown that using one exponential function instead of two is possible with negligible accuracy loss, [4].

A sketch of the near wake geometry is shown in Figure 1. The induction W at a blade section s at a time step i is found as the sum of the induced velocities due to all vortex arcs v trailed from a blade:

$$W_s^i = \sum_{v=1}^{N_v} W_{s,v}^i \tag{1}$$

The induced velocity due to an individual vortex arc is

$$W_{s,v}^i = W_{s,v}^{i-1} e^{-\Delta\beta/\Phi_{s,v}} + D_{w,s,v}\Delta\Gamma(1 - e^{-\Delta\beta/\Phi_{s,v}}) \tag{2}$$

where $\Delta\beta$ is the angle the blade rotates during a time step and Φ is a geometric parameter depending on the positions of vortex trailing point and blade section, as well as the helix angle of the trailed vortex arc. The trailed vortex strength, which depends on the radial gradient of the bound circulation, is $\Delta\Gamma$ and $D_{w,s,v}$ describes the induced velocity at section s due to a trailed vortex arc v with circulation 1 that starts directly at the blade. The advantage of using exponential functions is apparent: To obtain the induction at a new time step, the induction due to the newly trailed vortex element, the right term in Equation (2), is added to the exponentially decreasing induced velocity due to all previously trailed elements contained in $W_{s,v}^{i-1}$.

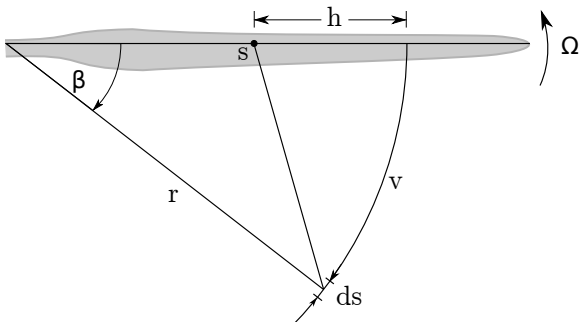

Figure 1. Sketch of the geometry in the near wake. The vortex arc v, trailed at radius r, induces axial (out-of-plane) and tangential (in-plane) velocities at the section s. The radial distance between vortex trailing point and section position is denoted h and $h > 0$ if the vortex is trailed outboard of the section. The angle β describes how far a vortex element with length ds has moved away from the blade. The figure is adapted from Pirrung et al., [6]. In practice, the blade is discretized into many sections and vortices are trailed from the root and tip and in between sections.

3. Model extension

In order to enable computation of standstill cases, a new definition of the angle β is necessary. The previous implementation used the projection of the trailed vortex filament in the rotor plane, which is not possible in standstill conditions. Thus the angle β is redefined:

$$\beta^* = \frac{v_{rel}\Delta t}{r}, \tag{3}$$

where v_{rel} is the relative velocity at which the vortex filament is trailed. If the trailed vorticity stays in the rotor plane, the old and new definitions are identical, $\beta = \beta^*$.

The new definition of β^* accounts for the differing element length trailed in one time step due to the downwind convection velocity. The axial and tangential components of the induced velocities due to the newest element, cf. Equation (2), can be determined based on the helix angle φ:

$$D_{w,s,v,axial} = D_{w,s,v}\cos\varphi \tag{4}$$

$$D_{w,s,v,tangential} = D_{w,s,v}\sin\varphi. \tag{5}$$

Because the near wake model is mainly meant to capture trailed vorticity effects close to the blade, the local inflow angle is used as helix angle φ. This inflow angle is computed based on the velocity triangle at the vortex trailing point and is affected by the free wind speed including turbulence, the movement of the blade and the induced velocities due to near and far wake. This way the near wake flow situation depends only on the velocities at the blade section, which is similar to how the 2D unsteady aerodynamics effects are computed, [1]. The time simulation of axial and tangential induction is then computed independently, so Equations (1) and (2) are evaluated twice for each section-vortex arc combination.

If the downwind convection velocity increases, the paths of the trailed vorticity change from circular (at zero convection speed) over helical (at moderate convection speed) to straight (at standstill). This influences both the steady state value of the induction from trailed vorticity and the dynamic behavior. Both of these can be modeled by changing the parameter Φ in Equation (2).

As described in [3], an optimal value of Φ can be computed. With this Φ_{opt}, the indicial function approximation computes the same steady state induced velocity as the Biot-Savart law:

$$\int_0^{pi/2}\left(\frac{\left(\frac{h}{r}\right)^2\left[1-\left(1-\frac{h}{r}\right)\cos\beta\right]}{\left(1+\left(1-\frac{h}{r}\right)^2-2\left(1-\frac{h}{r}\right)\cos\beta+(\beta\tan\varphi)^2\right)^{3/2}}\right)d\beta = \int_0^{pi/2}\left(1.359e^{-\beta/\Phi_{opt}}-0.359e^{-4\beta/\Phi_{opt}}\right)d\beta. \tag{6}$$

Here, r denotes the radial position where the vortex is trailed, and h the distance from the vortex trailing position to the radial position of the blade section where the induction is to be determined (positive if the section is inboard the vortex), cf. Figure 1. For straight vortices, Φ varies linearly with h/r

$$\Phi_s = \begin{cases} 0.788\frac{h}{r} & \text{for } 0 < h/r < 1 \\ -0.788\frac{h}{r} & \text{for } h/r < 0. \end{cases} \tag{7}$$

To ensure that the model can be used for straight vortices in standstill conditions and helical vortices in normal operation, a new $\Phi^\star$ is computed, that is a linear interpolation between Φ_s for straight vortices, Equation (7), and Wang and Cotons expression for circular vortices, [7]:

$$\Phi^\star = k_\Phi\Phi_s + (1-k_\Phi)\Phi, \tag{8}$$

where the interpolation k_Φ is a function of both h/r and the tangent of the helix angle. The straight and circular Φ approach each other for $h/r- > 0$, meaning for sections very close to vortex trailing points, where the influence of the vortex is large and an accurate computation of Φ is thus very important. Therefore the interpolation proposed in Equation (8) ensures good results for close positions, which would be difficult to achieve by direct curve fitting of Φ to the optimal value according to Equation (6).

For positive values of h/r, k_Φ can be approximated as

$$k_\Phi = a_{hr,1} + a_{hr,2}\varphi + a_{hr,3}\varphi^2 + a_{hr,4}\varphi^3 \tag{9}$$

$$a_{hr,i} = p_{i,1} + p_{i,2}\frac{h}{r} + p_{i,3}\left(\frac{h}{r}\right)^2 + p_{i,4}\left(\frac{h}{r}\right)^3 \tag{10}$$

For negative values of h/r:

$$k_\Phi = a_{hr,1} + a_{hr,2}e^{a_{hr,3}(\frac{\pi}{2}-\varphi)} + a_{hr,4}e^{-8(\frac{\pi}{2}-\varphi)} - a_{hr,2} - a_{hr,4} \tag{11}$$

$$a_{hr,i} = n_{i,1} + n_{i,2}e^{n_{i,3}\left(\frac{h}{r}\right)} + n_{i,4}e^{n_{i,5}\left(\frac{h}{r}\right)} - n_{i,4} - n_{i,2} \tag{12}$$

The values $n_{i,j}$ and $p_{i,j}$ are collected in the matrices **N** and **P**:

$$\mathbf{N} = \begin{pmatrix} 1.01933 & -0.13567 & 0.39552 & 0.08018 & 44.83475 \\ 12.98745 & 50.0 & 0.00235 & 11.31161 & 3935.34323 \\ -0.69016 & 101.23878 & -0.00154 & 3.99520 & 0.39454 \\ -0.26925 & 50.0 & -0.00248 & 0.40364 & 1.16610 \end{pmatrix} \tag{13}$$

$$\mathbf{P} = \begin{pmatrix} -1.64637 & 8.14821 & -12.17849 & 5.02653 & 21.77131 \\ -0.49901 & 6.08465 & -15.17120 & 14.82541 & -2.42319 \\ 3.90836 & -18.76623 & 39.12433 & -29.48701 & -60.29473 \\ -1.60623 & 7.42953 & -15.85948 & 11.68702 & -195.06087 \end{pmatrix} \tag{14}$$

Optimal and approximated values for Φ are shown for different helix angles ranging from 0 (circular arcs) to 89 degrees in Figure 2. The 89 degrees have been chosen because for 90 degrees the integral in Equation (6) can't be evaluated. It is shown clearly that the approximation gives a good representation of Φ across the range of helix angles. There are some deviations for $h/r \to 1$, which represents the influence of vortices close to the tip on the root sections. Because the deviations only influence roughly the innermost 5 % of the rotor radius, where often no aerodynamic profiles are installed, the quality of the approximation is acceptable.

4. Unsteady airfoil aerodynamics model

The 2D unsteady airfoil aerodynamics model in HAWC2 consists of both an attached flow model for the 2D shed vorticity effects and a dynamic stall model to predict unsteady flow separation, [1]. The attached flow model uses indicial functions assuming a flat plate. The dynamic stall model interpolates between a fully attached and fully separated airfoil polar, based on a time lagged separation point. The dynamic stall model does not include leading edge separation. The bound circulation necessary for the strength of the trailed vortices is determined by using an indicial function approach, where the quasi steady bound circulation is computed according to the quasi steady lift coefficient, [4]. This accounts for stall in the bound circulation computation.

5. Results

5.1. Elliptical wing

The case of an elliptical wing with a 10 meter span has been used previously to test the NWM, cf. [8, 6]. In these earlier publications, the wing was placed at the end of a very long, slowly rotating blade to ensure

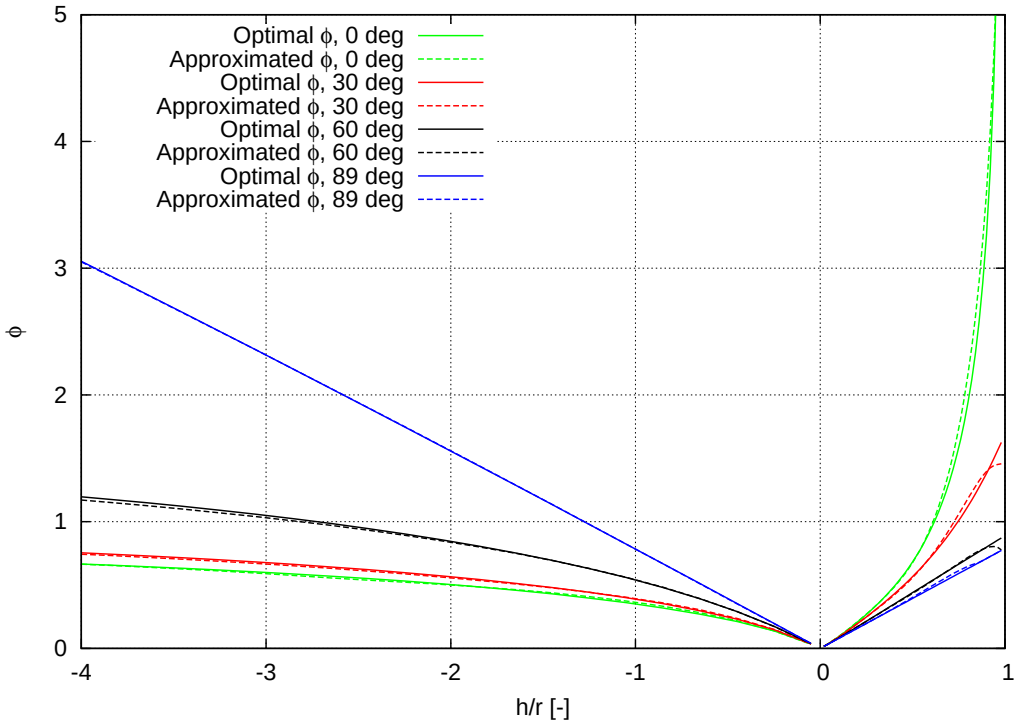

Figure 2. Approximation of phi at different helix angles compared to the optimal phi value.

an almost parallel inflow. In this work, the wing is instead mounted on a 0.5 meter long, non-rotating hub and is in a uniform inflow of 35 m/s. The previous publications prescribed an elliptical circulation distribution, but in this work the wing is modeled with a geometric AOA to the inflow of 5.45 degrees and a maximum chord length of 5.21 meters. The geometric AOA is defined as the angle of the local chord line with respect to the inflow direction in HAWC2, which corresponds to the wind tunnel center line in case of the Phase VI measurements discussed later. A lift gradient of 2π is used, which leads to the analytical result of a constant downwash of 1.5 m/s at the wing.

Figure 3 compares downwash at the lifting line computed from original and extended NWM with the analytical solution. The original model fails to predict the constant downwash in stand still, while the results from the extended model are in good agreement with the analytical solution.

5.2. NREL Phase VI rotor in stand still.

In all following comparisons, 'HAWC2' refers to HAWC2 stand still simulations. The BEM model and dynamic inflow model are disabled, because the BEM model is not valid in standstill and the dynamic inflow model models the unsteady behavior of the BEM induction. The 2D unsteady aerodynamics model containing shed vorticity and dynamic stall modeling as introduced in Section 4 is active.

In addition to the 2D unsteady aerodynamics model, the 'HAWC2 NW' simulations include the trailed vorticity modeling by the extended near wake model.

5.2.1. Non-pitching Besides measurements at operation the Phase VI experiment also contained measurements in standstill, some of which have been compared to CFD results by Johansen et al, [9] and Sørensen et al.,[10]. Here, some steady comparisons with measurements published in [9] are shown together with comparisons at lower geometric angle of attack.

The inflow speed in the cases presented here is 20 m/s, which results in a Reynolds number of 0.86 million at 47% blade radius. The Reynolds number varies along the blade with the chord length (ignoring

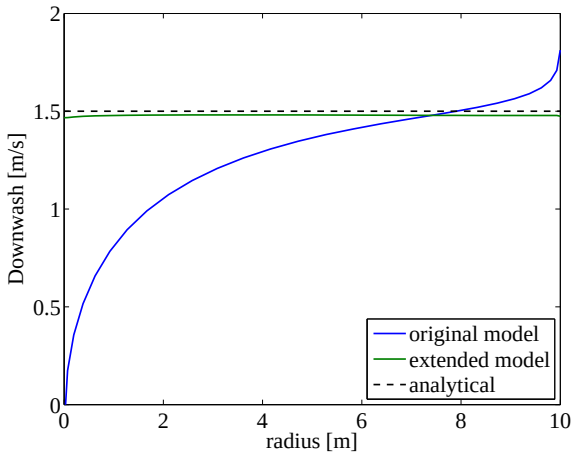

Figure 3. Results for an elliptical wing.

induced velocity effects on the Reynolds number), and the aerodynamic code interpolates accordingly between different airfoil polars.

A comparison of the radial distribution of the normal force coefficient is shown in Figure 4 at 3.5 and 18.2 degrees geometric AOA at 47% blade radius. At 3.5 degrees geometric AOA at the 47 % station, most of the blade is in attached flow. In this case, the near wake model predicts a radial distribution of the normal coefficient that agrees well with the measurements in terms of the radial load gradients, but there is an offset to the measurements. No explanation for this offset has been found. The results at the higher geometric AOA, where most of the blade is in stall, are shown in the right plot of Figure 4. In this case the near wake model can predict the root vortex well, but the agreement with the measurements becomes worse toward the tip, where the blade is in deep stall.

The steady state comparison of the tangential force coefficients in these cases in Figure 5 lead to the same conclusions. Again there appears to be an offset between near wake computations and measurements in the 3.5 degrees case. In the 18.2 degrees case the prediction of the root vortex by the near wake model is clear, but the agreement gets worse towards the stalled tip.

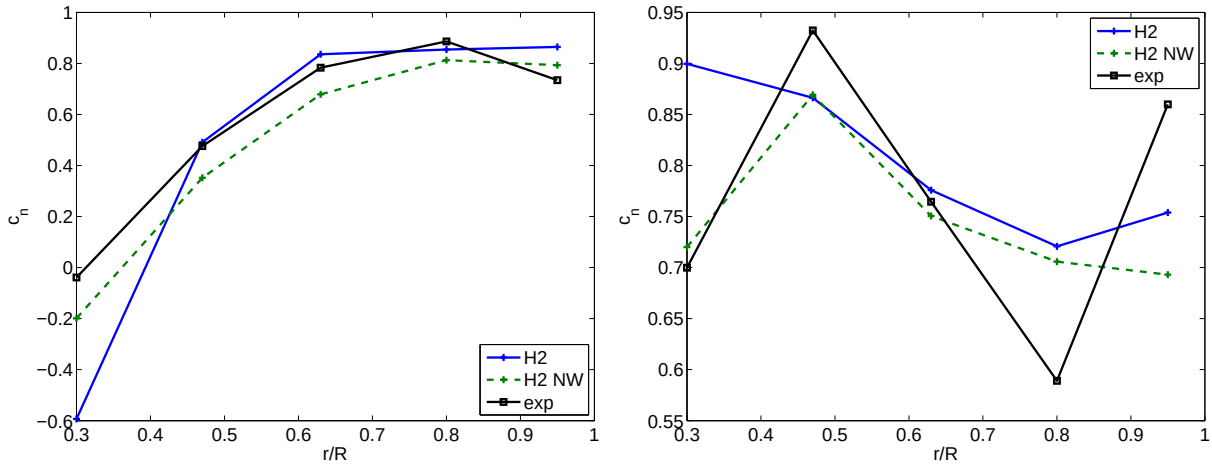

Figure 4. Radial distribution of normal force coefficients at 3.5 (left) and 18.2 (right) degrees geometric AOA at 47% blade radius. Results from HAWC2 (denoted H2) and HAWC2 including the extended near wake model presented in this paper (H2 NW) are compared to measurements.

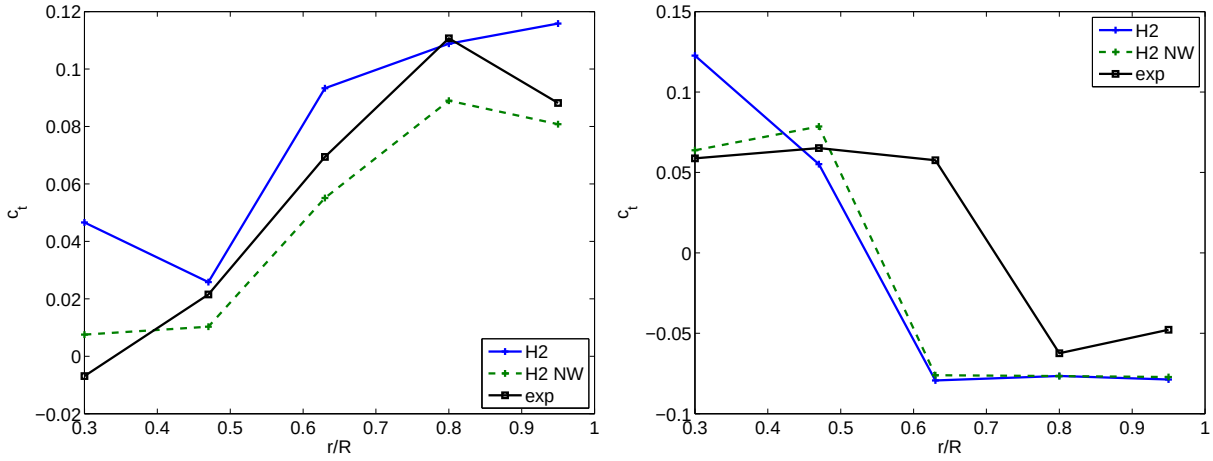

Figure 5. Radial distribution of tangential force coefficients at 3.5 (left) and 18.2 (right) degrees geometric AOA at 47% blade radius. Results from HAWC2 (denoted H2) and HAWC2 including the extended near wake model presented in this paper (H2 NW) are compared to measurements.

5.2.2. Pitching Two cases of a pitching blade are presented here: case O47010 with a mean geometric AOA at the 47% station of 3 degrees and a pitching amplitude of 2 degrees at a frequency of 0.739 Hz (reduced frequency $K = 0.0625$ at 47%) and case O47320 with a mean geometric AOA at the 47% station of 14 degrees and a pitching amplitude of 5.5 degrees at a frequency of 1.183 Hz (reduced frequency $K = 0.1$ at 47%). The free stream velocity in both cases is 23.3 m/s.

The normal force coefficient variation for the O47010 case are shown in Figure 6. The mean geometric AOA is only half a degree different than in the steady case in Figure 4, and almost the full blade is in attached flow. The unsteady simulation agrees with the steady simulation in an offset, where the HAWC2 NW results are below the measurements at every station but the blade tip. A comparison of the mean values would thus not lead to new conclusions. For easier dynamic comparison, the mean values of c_n have been substracted in Figure 6. The near wake modeling leads to improved agreement with the measurements everywhere except at the 63% station, where the differences between the predicted and measured loops are small. At the other radial stations HAWC2 NW predicts the loop openings and gradients much better than HAWC2. At the 80% station it is especially clear that the HAWC2 NW model predicts the exact position on the airfoil polar, while the actual (not geometric) AOA of the HAWC2 computations is too high. Thus the offset in the mean value is unexpected.

The c_t variations in Figure 7 show improved simulation results due to the NWM, at most blade stations except 47%. Similar as in the c_n comparison above, HAWC2 NW predicts gradients and loop openings that are very close to the measurements. The normal force coefficient loops for the O47320 case (14 degrees mean AOA at the 47% radial station) are shown in Figure 8. Because the amplitudes are larger and the mean AOA is higher in this case, the loops are more open and more nonlinear. Therefore the unsteady aerodynamics model have a larger influence on the mean values of c_n and c_t than in case O47010 and it has been chosen not to substract the mean values in the O47320 results. The flow is only attached at the 30% radial station, cf. Figure 8, and there HAWC2 NW predicts the c_n gradient more accurately than HAWC2. At the 47% radial station, HAWC2 NW predicts a slightly higher range of c_n, that is closer to the measurements. Also the shape of the loop predicted by HAWC2 NW agrees better with the measurements than that predicted by HAWC2, but both models do not reach as high maximum c_n values as the measurements. At the 63% station HAWC2 NW predicts a slightly more open loop than HAWC2 at up to 17 degrees geometric AOA, which is in better agreement with the measurements. Also in agreement is the increasing normal force coefficient towards higher AOA, which is not predicted by HAWC2. As at the 47% station, and also further outboard, the models underpredict the maximum measured c_n values. At both the 80% and 95% stations, the loops predicted by HAWC2 are narrowing

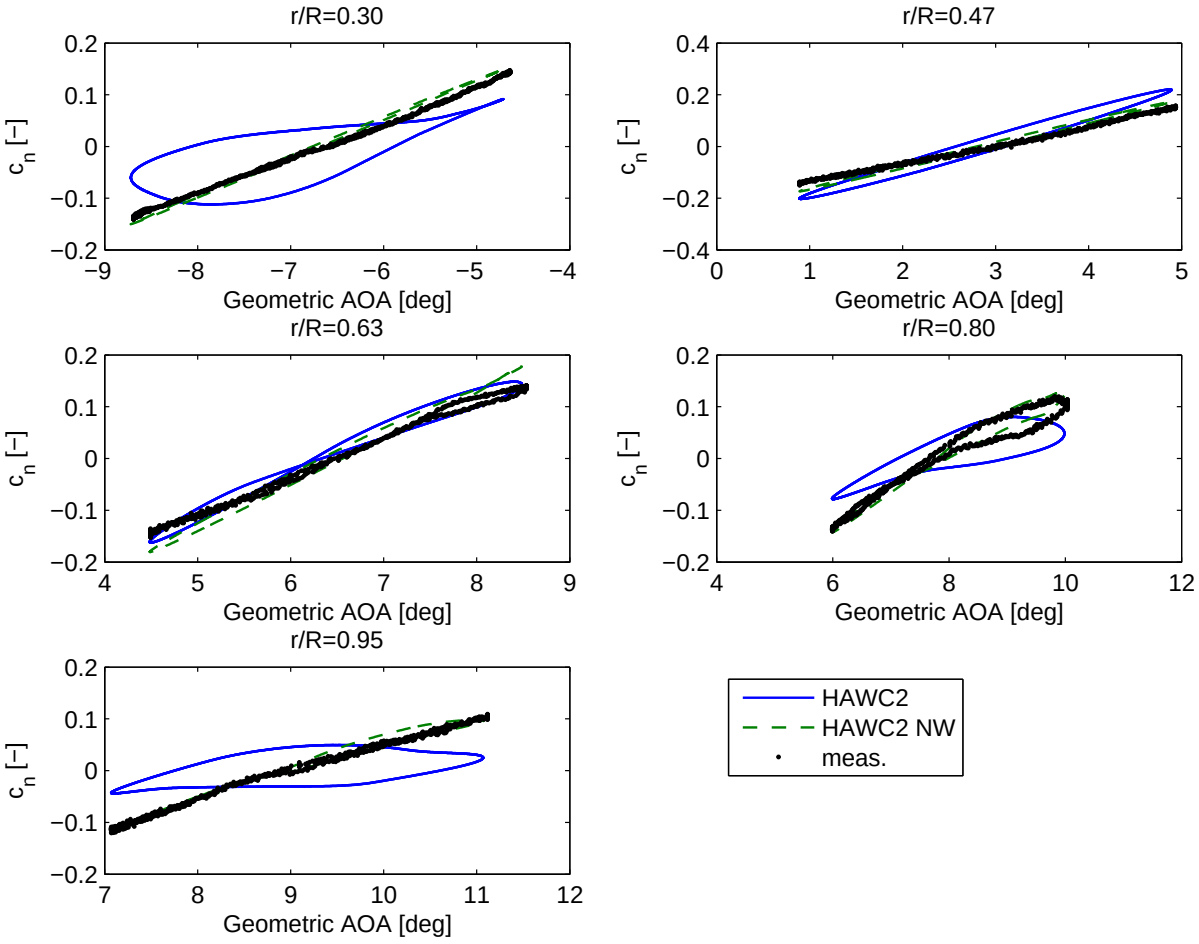

Figure 6. Case O47010, Variation about mean c_n

towards the high angles of attack. This is because the dynamic stall model interpolates between a fully attached and fully separated curve, cf. Section 4. At high angles of attack, where the flow is fully separated, the dynamic stall model becomes steady, because the separation point does not move any more, and accordingly the loops close. Due to the trailed vorticity in the HAWC2 NW computations, the local angles of attack at the radial stations close to the tip are lower than the geometric angles of attack, and therefore the flow is not yet considered fully separated. Thus the loops predicted by HAWC2 NW do not become more narrow towards high geometric AOA at the 80% and 95% stations. Even though the loop opening predicted by HAWC2 NW at the 95% radial station is closer to the measurements, the gradient of the c_n loop can not be predicted.

The loops of the tangential force coefficient in the O47320 case are shown in Figure 9. At the 30 % station in attached flow, HAWC2 NW clearly predicts a loop opening and gradient that agrees better with the measurements than the results from HAWC2. At the 47% radial station, HAWC2 NW predicts the form of the loop slightly better, but the opening in the measured loop is considerably larger. At the further outboard stalled stations there is generally a large disagreement between both codes and the measurements and it is difficult to state which codes' predictions agree better with the measurements.

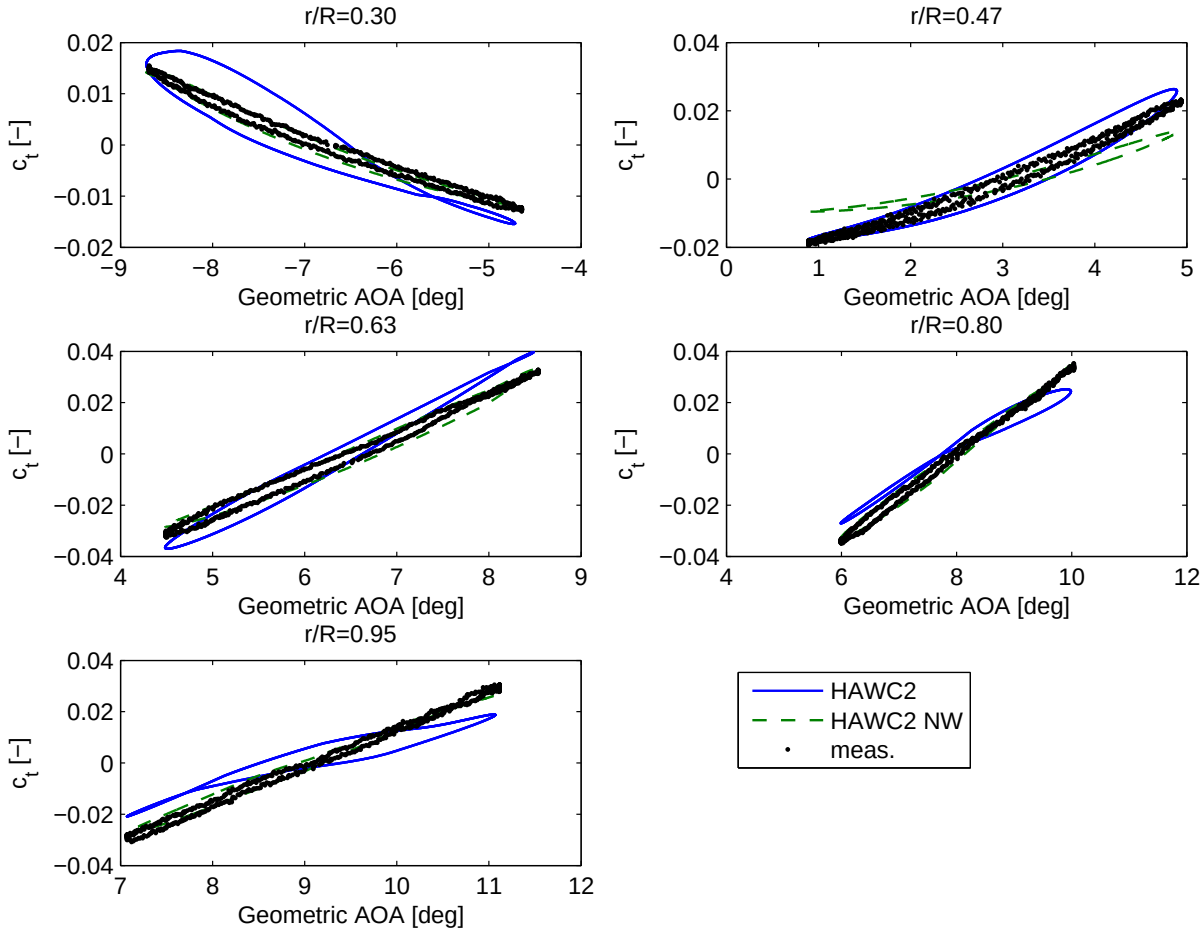

Figure 7. Case O47010, Variation about mean c_t

6. Conclusions

The near wake model has been extended to compute the induction due to trailed vorticity in standstill. Due to the twist distribution of a wind turbine blade and the larger effect of turbulence in standstill when compared to operational conditions, strong vortices can be trailed from any position along the span of the blade. Comparison with the analytical solution of a constant downwash for an elliptical wing shows good agreement with results from the extended near wake model, with the original model predicting large radial variations of the downwash.

Comparison with measurements from the NREL/NASA Ames phase VI experiment in attached flow conditions shows an unexplained offset between the steady state normal and tangential force coefficients measured and predicted by HAWC2 NW. However, the HAWC2 NW code predicts the effect of the trailed vorticity on the radial load gradients in steady state.

A comparison of the dynamic variation of the force coefficients for a sinusoidally pitching blade in attached flow shows that HAWC2 NW can predict dynamic loops that agree much better with the measurements than those predicted by HAWC2 on the major part of the blade. The agreement is improved both in terms of gradients and openings of the loops.

In a steady state comparison at high mean AOA, where the flow is separated at most of the blade, the near wake model can predict the root vortex at the inner part of the blade in attached flow. At the rest of the blade no clear improvement due to the added trailed vorticity modeling is visible. At the tip, which is in deep stall, the predicted normal force coefficient agrees worse with the measurements.

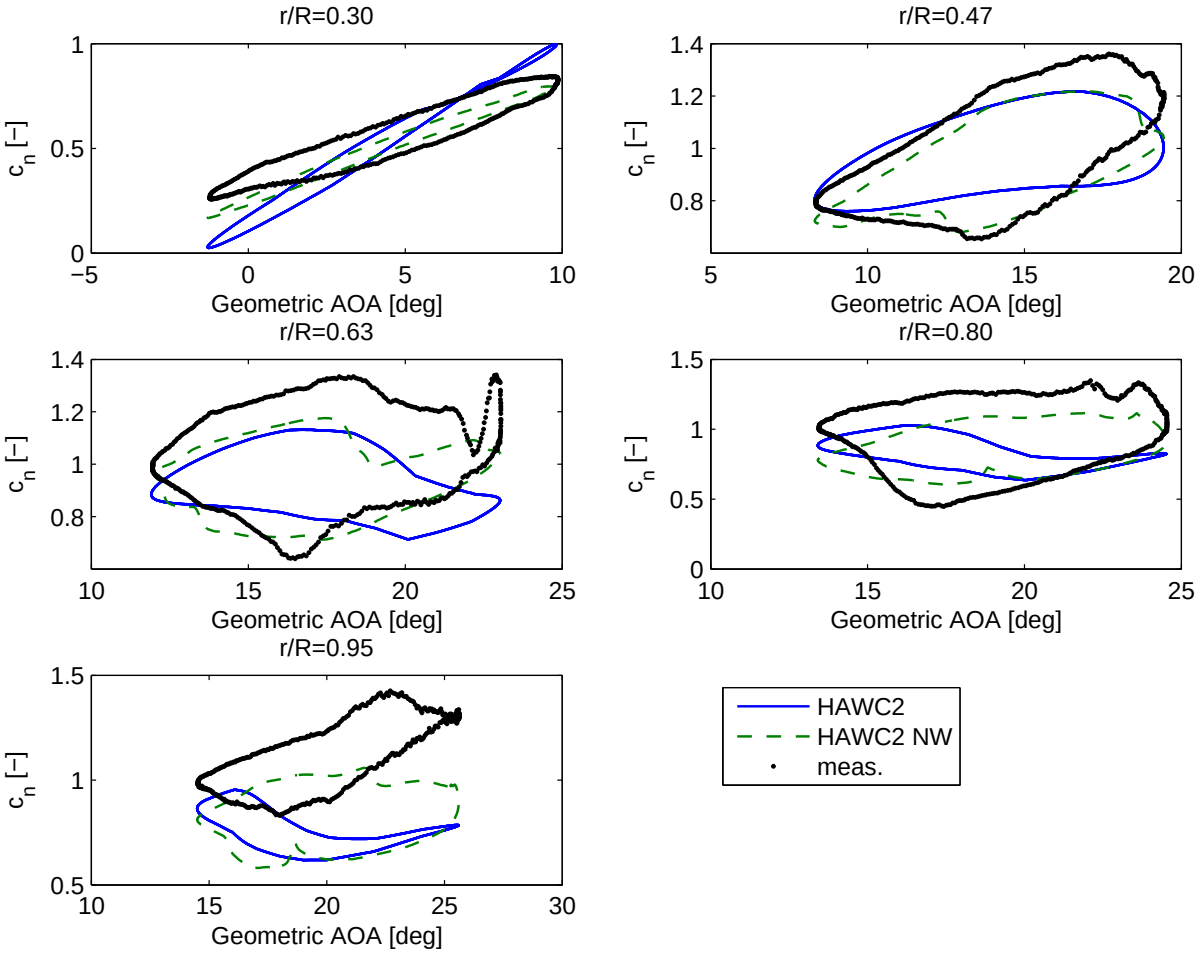

Figure 8. Case O47320, c_n

The unsteady comparison at high AOA shows a clear improvement at the inner part of the blade, which is in attached flow. Also on the outer part the openings of the c_n loops are predicted better by HAWC2 NW than HAWC2, mainly because the flow in the HAWC2 simulations is close to fully separated, where the dynamic stall model can not predict the dynamic behavior. The HAWC2 NW simulations predict lower AOAs close to the blade tip and thus the dynamic stall loops stay open. Even though the trailed vorticity modeling leads to improved predictions in this case, the basic weakness of the Beddoes-Leishman type dynamic stall model in deep stall should be adressed in future research. Further, the outboard c_t loops in stall are found to be difficult to model.

Acknowledgement
The work has been conducted within the project “Research and development of optimal wind turbine rotors under offshore wind conditions in China (OffWindChina)”, funded by “Det Strategiske Forskningsråd ved Programkomiteen for Bæredygtig Energi og Miljø”, contract 12-130590. http://www.offwindchina.vindenergi.dtu.dk/

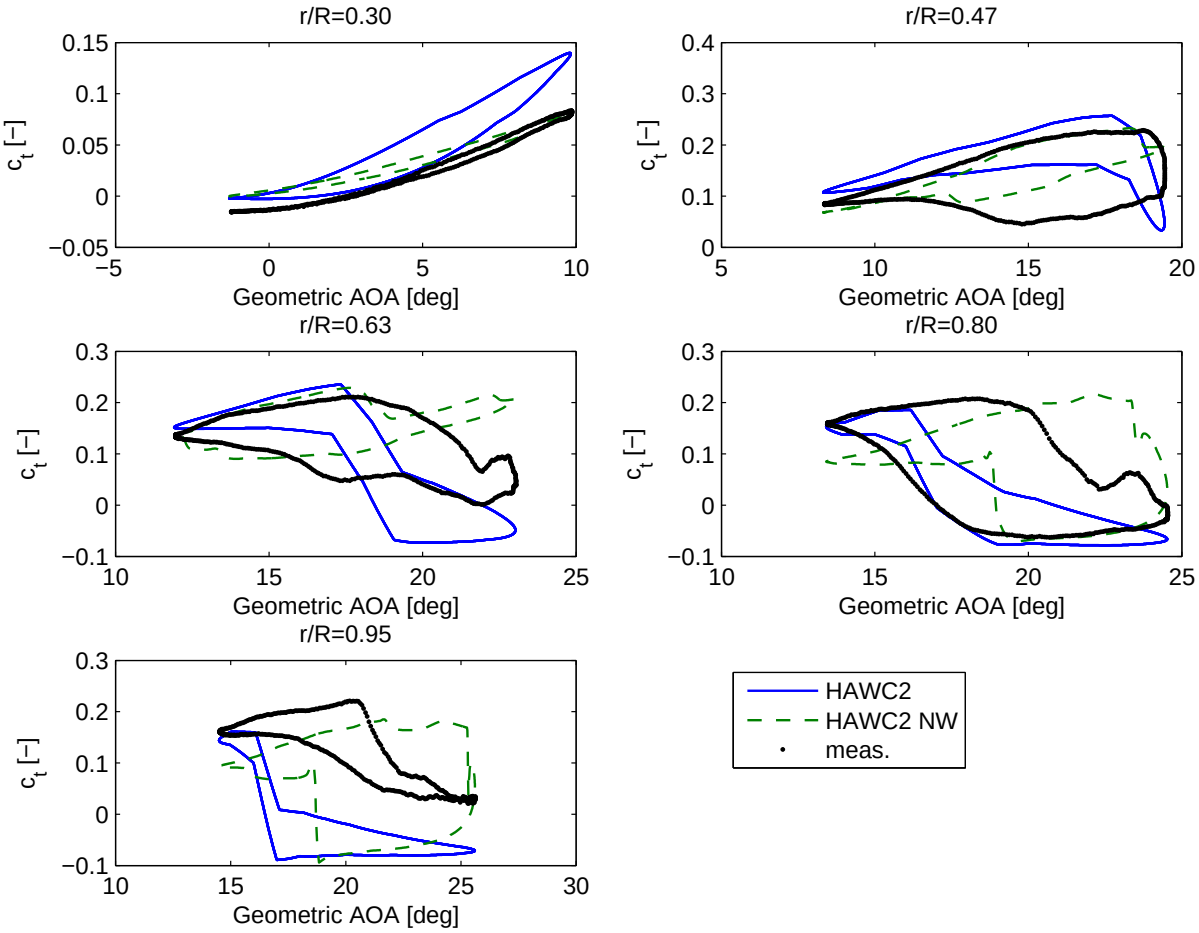

Figure 9. Case O47320, c_t

References

[1] M. H. Hansen, M. Gaunaa, and H. Aa. Madsen. *A Beddoes-Leishman type dynamic stall model in state-space and indicial formulations*. Risø-R-1354, Roskilde, Denmark, 2004.

[2] Torben J. Larsen and Anders Melchior Hansen. *How 2 HAWC2, the user's manual*. Denmark. Forskningscenter Risoe. Risoe-R-1597. 2007.

[3] G. R. Pirrung, H. A. Madsen, T. Kim, and J. Heinz. A coupled near and far wake model for wind turbine aerodynamics. *Wind Energy*, 2016. doi:10.1002/we.1969.

[4] G. Pirrung, V. Riziotis, H. Madsen, M. Hansen, and T. Kim. Comparison of a coupled near and far wake model with a free wake vortex code. *Wind Energy Science Discussions*, 2016:1–28, 2016.

[5] MM Hand, DA Simms, LJ Fingersh, DW Jager, JR Cotrell, S Schreck, and SM Larwood. *Unsteady aerodynamics experiment phase VI: wind tunnel test configurations and available data campaigns*. NREL/TP-500-29955, National Renewable Energy Laboratory Golden, Colorado, USA, 2001.

[6] G R Pirrung, M H Hansen, and H A Madsen. Improvement of a near wake model for trailing vorticity. *Journal of Physics: Conference Series*, 555(1):012083, 2014.

[7] T. Wang and F. N. Coton. A high resolution tower shadow model for downwind wind turbines. *Journal of Wind Engineering and Industrial Aerodynamics*, 89:873–892, 2001.

[8] H. Aa. Madsen and F. Rasmussen. A near wake model for trailing vorticity compared with the blade element momentum theory. *Wind Energy*, 7:325–341, 2004.

[9] J. Johansen, N. N. Sørensen, J. A. Michelsen, and S. Schreck. Detached-eddy simulation of flow around the nrel phase vi blade. *Wind Energy*, 5(2-3):185–197, 2002.

[10] Niels N. Sørensen and Scott Schreck. Computation of the national renewable energy laboratory phase-vi rotor in pitch motion during standstill. *Wind Energy*, 15(3):425–442, 2012.